AALBORG UNIVERSITY

Mass Transfer and Pressure Drop Similarities in Oriented, Periodically Confined Channels

Aschmoneit, Fynn Jerome

Link to publication from Aalborg University

Citation for published version (APA):
Aschmoneit, F. J. (2025). *Mass Transfer and Pressure Drop Similarities in Oriented, Periodically Confined Channels.* (pp. 1-14). arXiv. https://doi.org/10.48550/arXiv.2502.07091

Mass Transfer and Pressure Drop Similarities in Oriented, Periodically Confined Channels

F. J. Aschmoneit

Department of Mathematical Sciences, Aalborg University, Copenhagen, Denmark

Abstract

This study presents a detailed quantification of how flow orientation affects mass transfer and frictional resistance in periodically confined channels, offering novel insights into the physical similarity relations governing these phenomena. We constitute that the Sherwood number and friction factor adhere to universal scaling laws of the form $Sh = A\Big(1 + B \sin(2\alpha)\Big) Re^{\frac{1}{2}}$ and $f = A\Big(1 + B \sin(2\alpha)\Big) Re^{-\frac{1}{2}}$, where α depicts the orientation of the periodically confined channel.

It is found that the flow orientation and the cross flow velocity independently affect both, the Sherwood number and the friction factor. A key contribution of this work is the explicit characterization of the flow orientation: a 45° rotation of the flow relative to the spacer structure increases the Sherwood number by nearly 25%, while the friction factor rises by approximately 20%. These findings highlight a fundamental trade-off between mass transfer enhancement and flow resistance, suggesting that any process optimization must carefully balance the gains in mixing efficiency against the increased energy dissipation. This study provides a robust framework for further investigations into how periodic geometrical constraints influence transport processes in complex flow systems.

Keywords: Physical similarity relations, mass transfer, friction factor, flow orientation, scaling laws, confined channels, transport phenomena.

1. Introduction

The mixing capability and the pressure drop are largely affected by the channel flow velocity. These are commonly described in terms of the Sherwood number and the friction number, respectively. The Sherwood number scales with the square root of the Reynolds number, $Sh \sim Re^{\frac{1}{2}}$. The friction factor, on the other hand, scales reciprocal square root of the Reynolds number, $f \sim Re^{-\frac{1}{2}}$. It is of interest, how the respective proportionality constant changes with respect to changes in flow orientation. Earlier studies suggest that a 45 deg angle is advantageous for the solute mixing. But this is often a qualitative observation. How exactly is the orientation angle affecting the Sherwood number and the friction number?

In the context of membrane science, different separation processes are commonly analyzed based on similarity relations of Sherwood and friction numbers.

Most commonly, in reverse osmosis, the design of the spiral-wound module is analyzed in various studies, see for example Schwager et al. (1980), Winograd et al. (1973), Focke (1983), Mokhtar et al. (2021), Aschmoneit and Hélix-Nielsen (2022). The pressure-retarded osmosis process is not related to a specific module design. Hence, the similarity relations of different designs have been analyzed towards module optimization, see Ng et al. (2023), Benjamin et al. (2022) Aschmoneit and Hélix-Nielsen (2021). The hollow fiber design is applied in membrane applications, such as forward osmosis Aschmoneit and Hélix-Nielsen (2020a) or in gas

---

Email address: `fynnja@math.aau.dk` (F. J. Aschmoneit)

separation, see He and Zhang (2019), or in heat exchangers Bohacek et al. (2021). These studies are examples of process quantifications based on similarity relations.

In this study we want to determine how the proportionality constants in the similarity relations above depend on the orientation of the flow in the periodically confined channel. We propose that the similarity coefficients of the form $A(1 + BQ(\alpha))$. Figure 1 depicts the spacer orientation is defined as the rotation from the head-on direction. The function $Q(\alpha)$ is must be symmetric with respect to the orientation angle, i.e. $Q(-\alpha) = Q(\alpha)$. Furthermore, since the geometry has a 90°-rotational symmetry, therefore $Q(\alpha + 90°) = Q(\alpha)$. We therefore propose $Q(\alpha) = \sin(2\alpha)$, for $\alpha \in [0°, 90°]$. Our template similarity relations are:

$$Sh = A\left(1 + B\,\sin(2\alpha)\right)Re^{\frac{1}{2}} \tag{1}$$

$$f = A\left(1 + B\,\sin(2\alpha)\right)Re^{-\frac{1}{2}} \tag{2}$$

We consider a flat channel of height H. The channel is constricted by a regular mesh of cylindrical rods. Along the bottom wall the rods run parallel at a distance of L. Similarly, at the top wall, the rods run parallel at a distance of L. Top- and bottom rods run perpendicular to each other. The strands extend to $3/5$ of the channel height, i.e. the strand diameter is defined as $D = 3/5\,H$. At the rod intersections top- and bottom rods interfere with each other. This constricted channel can be decomposed into periodic cells of rod segments. Figure 1 shows an illustration of the mesh of intersecting rods.
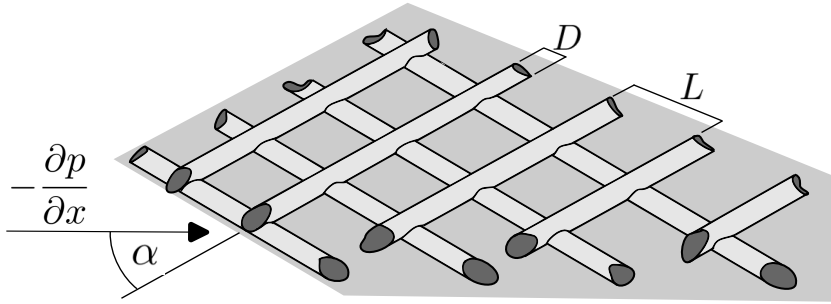

Figure 1: Sketch of channel. angle of attack, mirror picture, include x direction

In non-circular, uniform channels the hydraulic diameter d_h corresponds to the hypothetical diameter of a circular pipe with equivalent pressure drop. Hence, its value depends on the channel's cross-sectional geometry and is equated as four times the cross-sectional area, divided by the wet cross section perimeter. Similarly, in non-uniform channels, the hydraulic diameter is commonly defined as four times the void volume, V_{wet}, divided by the area of wet channel boundary, A_{wet}:

$$d_h = \frac{4V_{\text{wet}}}{A_{\text{wet}}} \tag{3}$$

The wet volume is defined as the difference of the empty channel volume and the volume occupied by the rods. The area of the wet channel boundary is defined as the quadratic top and bottom boundaries, plus the area of the rods. In the case of intersecting rods, i.e. if $2D > H$, we have to account for the intersection volume, which reduces both, the effective wet volume, and the wet surface area. Figure ?? illustrates that intersection volume V_{int}.

$$V_{\text{wet}} = \underbrace{HL^2}_{\text{empty channel}} - \underbrace{\frac{\pi}{2}D^2L}_{\text{two rods}} \tag{4}$$

2

$$A_{\text{wet}} = \underbrace{2L^2}_{\text{top, bottom boundaries}} + \underbrace{2\pi DL}_{\text{two rods}} \tag{5}$$

The intersection of the cylinders is defined through:

$$\delta_C = \frac{2D - H}{D} = 2 - \frac{H}{D} \tag{6}$$

We define the hydraulic diameter and the the porosity for a $28mil$ and a $34mil$ spacer, which are commonly used in membrane filtration systems:

Table 1:

configuration	$L(\mu m)$	$H(\mu m)$	δ_C	$D(\mu m)$	$d_h(\mu m)$
28 mil	2822	711	1/3	427	827
34 mil	3629	867	1/3	520	1034

The flow through the spacer filled channel is driven by a constant pressure gradient. In the following, it is assumed, that this driving pressure gradient is directed in the $-\hat{e}_x$ direction, imposing a bulk mass flow in the $\hat{e}_x$ direction. Hence, along the $\hat{e}_x$ direction the pressure gradient has a constant term $-\beta$:

$$\partial_x P = \partial_x p - \beta, \tag{7}$$

The flow through the spacer channel is in the laminar region, $Re < 250$, and therefore, the flow will assume a fully developed profile, influenced by the periodically repeating spacer filaments. The existence of a steady-state solution is therefore assumed. Furthermore, the flow is assumed incompressible and Newtonian. Under these assumptions, the Navier-Stokes equations are:

$$u(\partial_x u) + v(\partial_y u) + w(\partial_z u) = -\frac{1}{\rho}\partial_x p + \nu(\partial_{xx} + \partial_{yy} + \partial_{zz})u + \frac{\beta}{\rho}$$

$$u(\partial_x v) + v(\partial_y v) + w(\partial_z v) = -\frac{1}{\rho}\partial_y p + \nu(\partial_{xx} + \partial_{yy} + \partial_{zz})v \tag{8}$$

$$u(\partial_x w) + v(\partial_y w) + w(\partial_z w) = -\frac{1}{\rho}\partial_z p + \nu(\partial_{xx} + \partial_{yy} + \partial_{zz})w$$

Furthermore, it is assumed that the solute concentration has a negligible effect on the water density. The mass conservation is then given by the continuity equation:

$$\partial_x u + \partial_y v + \partial_z w = 0 \tag{9}$$

It is assumed that the solute field is passive, i.e. the solute concentration does not affect the flow field. Under this assumption the solute transport depends on the steady-state velocity field and the solute's diffusion coefficient D:

$$(u\partial_x + v\partial_y + w\partial_z)s - D(\partial_{xx} + \partial_{yy} + \partial_{zz})s = 0 \tag{10}$$

In this study we assume a kinematic viscosity $\nu = 1 \times 10^{-6} m^2/s$ and a diffusion coefficient of NaCl in water $D = 1.49 \times 10^{-9} m^2/s$, as stated in Vitagliano and Lyons (1956).
The velocity field across the periodic cell also periodic. The solute concentration is increasing along the feed channel, and therefore not periodic across the periodic spacer cell. To circumvent this effect, a normalized, periodic solute concentration is applied. In Patankar et al. (1977), a normalized, periodic temperature is

3

defined for the description of heat transport in periodically changing ducts. The similarity of heat transport and solute transport allows to define a normalized solute concentration as:

$$s = \frac{c(x,y) - c_w}{c_b(x) - c_w},$$

(11)

where $c(x,y)$ is the local concentration, c_w is the constant wall concentration and c_b is a reference concentration. We treat s as a periodic variable, and since $\partial_n s \sim \partial_n c$, we do not need to convert the relative concentration into an absolute concentration and directly measure the solute mixing from the periodic concentration.

2. Computational Setup

The computational mesh was created using OpenFOAM's 'blockMesh' tool. Exploiting the two symmetry planes in the geometry reduces the mesh development to one quarter of the domain, which was then mirrored across the symmetry planes. Figure 2 (top,left) illustrates the block design used for mesh generation. The periodic cell geometry was discretized using hexahedral cells, with boundary layers of increased resolution near the spacer and membrane surfaces, as shown Figure 2.

A Grid Convergence Index (GCI) study was performed on the *d28m* geometry to quantify spatial discretization error convergence. The results suggested that the ideal mesh resolution for the smaller *d28m* geometry could also be applied to the larger *d34m* geometry. The GCI simulations were conducted with a prescribed pressure gradient to achieve a bulk flow velocity of approximately $20\,\text{cm/s}$ and a mesh orientation of $45°$. A bulk discretization of $140\,cells/\text{mm}$ and 14 boundary layers with a growth rate of 1.1 resulted in a discretization error of less than 1%. For the *d28m* geometry, this resolution produced a mesh of approximately 25 million cells.
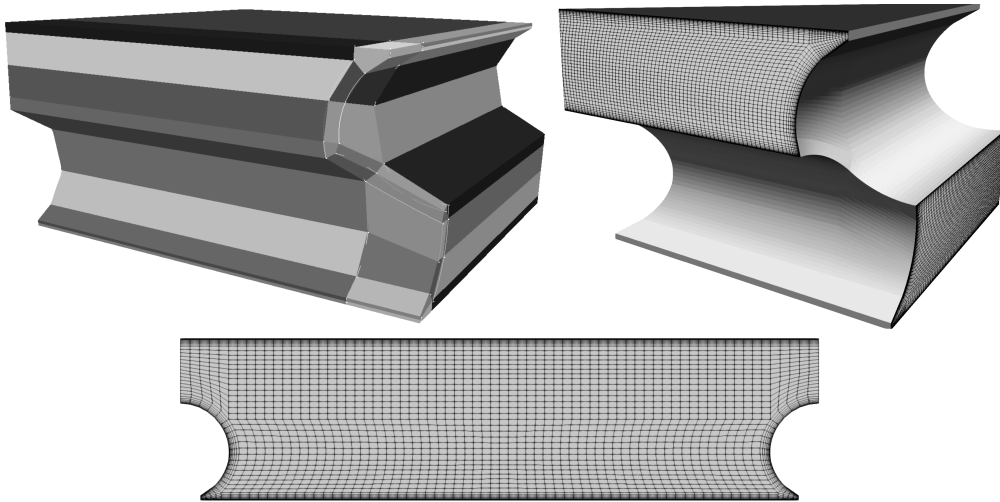

Figure 2: Computational mesh at intersection of traversing rods. Left one to supplementary material, intersection $\delta_C = 1/3$

The setup involves open flow faces where velocity and scalar variables are subject to pairwise periodic conditions. Note that although the absolute pressure P is not periodic, the dynamic pressure p is, as described in Equation 7. At the spacer, a no-slip condition is applied to velocity, and no-gradient conditions are applied to the scalar variables. For the top and bottom walls, a no-slip condition is applied to velocity, no-gradient for pressure, and the solute concentration is fixed to a value of 1. The initial field has the bulk concentration

set to zero, resulting in a solute difference $\Delta s = 1$. The cross flow is established using a prescribed pressure gradient to drive the flow towards a target cross-flow velocity, which is achieved using OpenFOAM's 'meanVelocityForce' feature.

Figure 3 indicates the solute mixing in terms of the local gradient of scalar concentration changes as the gross cross flow changes its orientation. Here, the darker areas indicate areas of low scalar gradients and poor mixing.
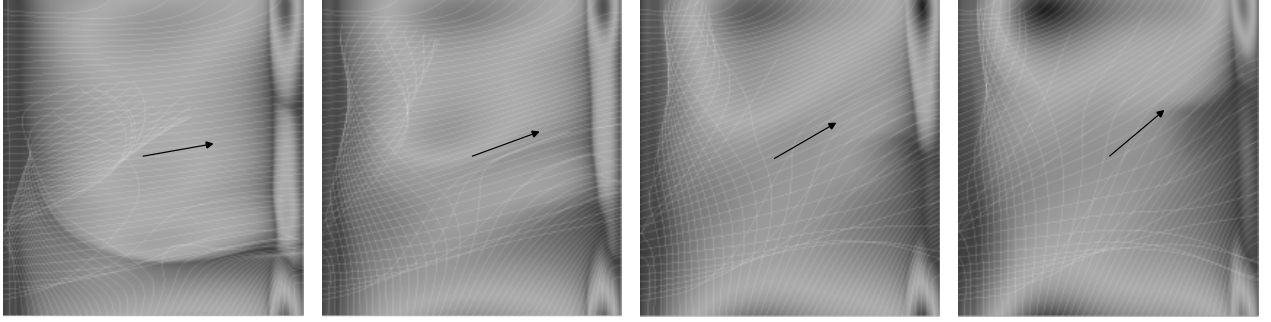

Figure 3: Map of scalar solute gradient. Brighter shades indicate greater gradient. Areas with dark shades indicate zones of poor mixing. The arrow indicate the overall flow directions $\alpha \in \{10°, 20°, 30°, 40°\}$

The solute mixing is quantified by averaging the local magnitudes of the non-dimensional scalar gradient in the direction normal to the boundary, see equation (12). This function was implemented as an OpenFOAM function object. The 'wallNormalScalarGrad' implementation is found here[1].

$$\frac{\partial_n s}{\Delta s} = \frac{1}{\Delta s \, A_{top,bottom}} \sum_{i:\text{top,bottom faces}} |\partial_n s_i| \, A_i \tag{12}$$

The pressure drop is quantified through the integral shear forces on the surfaces. OpenFOAM's incompressible 'wallShearStress' method produces a vector field S_i of the local reduced shear stress. These are averaged over all (wet) boundary faces A_i.

$$\frac{\tau}{\rho} = \frac{1}{A_{wet}} \sum_{i:\text{wall faces}} |S_i| \, A_i \tag{13}$$

Table 2 indicates the operation conditions in terms of cross flow and flow orientation, together with their resulting solute mixing and shear forces, according to equations (12, 13).

---

[1]`https://bitbucket.org/FynnAschmoneit/wallnormalscalargrad/src/master/wallNormalScalarGrad/`

orientation α [deg]	cross flow U [$cm\,s^{-1}$]	scalar normal grad $\partial_n s/\Delta s$ [$10^2\ m^{-1}$]		red. wall shear force τ/ρ [$10^{-6}\ m^2 s^{-2}$]	
		d28m	**d34m**	**d28m**	**d34m**
0	5	271	245	635	532
0	10	382	357	1588	1385
0	15	475	435	2913	2572
0	20	552	503	4529	4025
10	5	309	276	693	581
10	10	427	386	1714	1490
10	15	518	471	3122	2752
10	20	590	537	4847	4302
20	5	331	294	745	622
20	10	450	405	1823	1580
20	15	554	496	3325	2917
20	20	643	571	5182	4569
30	5	344	306	773	645
30	10	473	427	1883	1634
30	15	580	525	3422	3006
30	20	679	611	5314	4703
40	5	351	312	786	656
40	10	475	432	1896	1640
40	15	576	535	3432	3008
40	20	673	631	5330	4704
-	5	142	112	45	37
-	10	181	156	90	75
-	15	214	181	148	128
-	20	236	206	219	196

Qualitatively, the data suggests that shear forces are one order of magnitude greater in spacer filled channel, compared to the empty channel. The narrow channel causes a greater shear stress and greater orientation angles cause greater shear stress. Similarly, the solute mixing is increased by the spacers, though not by one order of magnitude. The greater cross flow velocity and greater spacer orientation also increase the solute mixing. A systematic analysis of these effects follows here.

3. Methodology

The data in Table 2 are translated to the Sherwood number and the friction factor through $Sh = \frac{d_h}{\Delta c}\frac{\partial c}{\partial n}$ and $f = \frac{8\tau}{\rho U^2}$, respectively. In the following, we illustrate how the similarity functions (1, 2) are fitted against these data. The general methodology is rooted in fitting the linear function $aX + bY$, with the independent vector variables X, Y, and the coefficients a, b, against the data encoded in vector Z. The least-square solution is found by minimizing the sum of the squared residuals:

$$\chi^2 = \sum_{i=1}^{MN} (Z_i - aX_i - bY_i)^2$$
$$= (Z - aX - bY) \cdot (Z - aX - bY)$$

(14)

6

with:

$$\frac{\partial}{\partial a}\chi^2 = -2X \cdot (Z - aX - bY)$$

$$\frac{\partial}{\partial b}\chi^2 = -2Y \cdot (Z - aX - bY),$$

where the dot denotes the inner product of the vector variables. The least-square solution result from $\partial_a\chi^2 = 0$ and $\partial_b\chi^2 = 0$. This yields the following equation system, which is readily solved for (a, b).

$$\begin{pmatrix} X \cdot X & X \cdot Y \\ X \cdot Y & Y \cdot Y \end{pmatrix} \begin{pmatrix} a \\ b \end{pmatrix} = \begin{pmatrix} X \cdot Z \\ Y \cdot Z \end{pmatrix} \tag{15}$$

Because of missing uncertainties for the measurements in Z, we assess the goodness-of-fit using the mean of the data vector $\bar{Z}$, with $\sigma^2 = (Z - \bar{Z}) \cdot (Z - \bar{Z})$, as:

$$R^2 = 1 - \frac{\chi^2}{\sigma^2} \tag{16}$$

In order to apply the least-square fitting in equations (14-16) to the different data sets in table 2, we need to linearize the respective scaling functions.

Analysis of Sherwood scaling with oriented spacers in channel
The Sherwood number scaling in the oriented spacer-filled channel is analyzed for both configurations individually, and also jointly. The scaling equation (1) is first linearized in the form $aX + bY$, and then subjected to least-square fitting (15). Here, the independent variables (X, Y) are constructed from the independent variables (Re, α). Let $Q = sin(2\alpha)$ be the rotation variable, we can then linearize the scaling relation (1) as:

$$Sh = \underbrace{A}_{a} \underbrace{Re^{\frac{1}{2}}}_{X} + \underbrace{AB}_{b} \underbrace{QRe^{\frac{1}{2}}}_{Y} \tag{17}$$

Similar cross flow velocities in both configurations translate to different Reynolds numbers, as a consequence of the different hydraulic diameters. Let $N \in \{4, 8\}$ be the number of distinct Reynolds number values, considering the cases of regarding only one, or both configurations simultaneously. Let $M = 5$ be the number of distinct values of the rotation variable Q, relating to the different angles in Table 2. Let X be the vector of M consecutive repetitions of the N distinct velocity components. The vector Y is constructed by the values of X, where each set of N consequent entries are multiplied with a distinct value of the M rotation variables. The vector Z contains the Sherwood numbers related to the 'scalar normal grad' column in Table 2.

$$\begin{aligned} X = &\Big(\underbrace{Re_1^{\frac{1}{2}}, Re_2^{\frac{1}{2}}, ..., Re_N^{\frac{1}{2}}}_{1}, \quad \underbrace{Re_1^{\frac{1}{2}}, Re_2^{\frac{1}{2}}, ..., Re_N^{\frac{1}{2}}}_{2}, \quad , ..., \quad \underbrace{Re_1^{\frac{1}{2}}, Re_2^{\frac{1}{2}}, ..., Re_N^{\frac{1}{2}}}_{M} \Big) \\ Y = &\Big(\underbrace{Q_1 X_1, Q_1 X_2, ..., Q_1 X_N}_{1}, \quad \underbrace{Q_2 X_{N+1}, Q_2 X_{N+2}, ..., Q_2 X_{2N}}_{2}, \quad , ..., \\ &, ..., \quad \underbrace{Q_M X_{(M-1)N+1}, Q_M X_{(M-1)N+1}, ..., Q_M X_{MN}}_{M} \Big) \\ Z = &\Big(Sh_1, Sh_2, ..., Sh_{MN} \Big) \end{aligned} \tag{18}$$

The scaling law coefficients (A, B) in equation (1) are then evaluated from the least-square coefficients (a, b) as $A = a$ and $B = b/a$. Table 3 summarizes the resulting scaling coefficients, together with the respective

goodness-of-fit values, according to equation (16), and Figure 4 illustrates the respective scaling law, together with the Sherwood number data. It is emphasized once more, that all data points in a given figure were fitted in one go, hence, the distinct lines in one figure result from just one single fit.

Table 3: Least-square coefficients and goodness-of-fit of Sherwood number scaling (1)

configuration	A	B	R^2 [%]
28 mil	3.542	0.244	99.6
34 mil	3.598	0.244	99.8
collective	3.573	0.244	99.6

The goodness-of-fit values indicate that the data is excellently described by the scaling law (1). The cross-flow velocity and the flow orientation influence the Sherwood number independently. Their effects are accurately represented by $Re^{1/2}$ for cross-flow velocity and $\sin(2\alpha)$ for the angle of attack. The coefficient for the flow orientation, B, is similar in both configurations, while the universal coefficient A varies only marginally between them. Therefore, a unified description of both configurations is practicable.

Given the excellent agreement when fitting both configurations together, it appears that the hydraulic diameter of the channels does not influence the Sherwood number. In fact, when dividing the universal coefficient A with the respective $(dh/\Delta l)^{\frac{1}{2}}$ factor, the discrepancy between the scaling coefficients becomes greater.

Notably, the flow orientation greatly affects the Sherwood number: Relating the coefficient B relates to unity, indicates that a 45° angle increases the Sherwood number by nearly 25%. This finding holds for all cross-flow velocities, highlighting the decoupling of flow orientation and velocity.
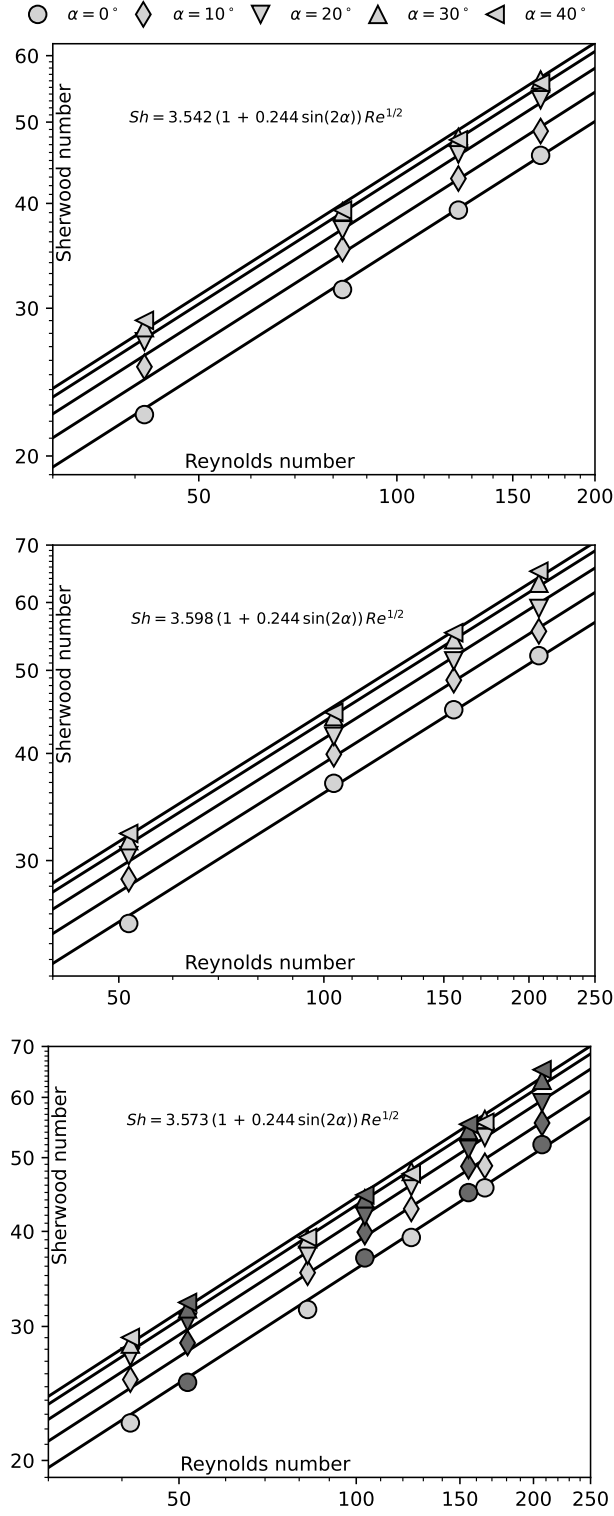
Figure 4: Sherwood number fits. Top: 28 mil config, Middle: 34 mil config, Bottom: joint configurations

Friction factor, spacer-filled

Similarly to the case of the Sherwood number, we linearize the the scaling law for the friction factor (2) with the independent variables (X, Y):

$$f = \underbrace{A}_{a} \underbrace{Re^{-\frac{1}{2}}}_{X} + \underbrace{AB}_{b} \underbrace{QRe^{-\frac{1}{2}}}_{Y}, \tag{19}$$

As seen in Figure 5, the friction numbers for the low cross flow velocities follow a different scaling behavior. We therefore exclude these in the fits. The number of distinct different Reynolds numbers is therefore $N = \{3, 6\}$, depending if only one configuration, or both configurations are considered.

$$
\begin{aligned}
X =& \Big(\underbrace{Re_1^{-\frac{1}{2}}, Re_2^{-\frac{1}{2}}, ..., Re_N^{-\frac{1}{2}}}_{1}, \quad \underbrace{Re_1^{-\frac{1}{2}}, Re_2^{-\frac{1}{2}}, ..., Re_N^{-\frac{1}{2}}}_{2}, \quad, ..., \quad \underbrace{Re_1^{-\frac{1}{2}}, Re_2^{-\frac{1}{2}}, ..., Re_N^{-\frac{1}{2}}}_{M} \Big) \\
Y =& \Big(\underbrace{Q_1 X_1, Q_1 X_2, ..., Q_1 X_N}_{1}, \quad \underbrace{Q_2 X_{N+1}, Q_2 X_{N+2}, ..., Q_2 X_{2N}}_{2}, \quad, ..., \\
& \quad, ..., \quad \underbrace{Q_M X_{(M-1)N+1}, Q_M X_{(M-1)N+1}, ..., Q_M X_{MN}}_{M} \Big) \\
Z =& \Big(f_1, f_2, ..., f_{MN} \Big)
\end{aligned} \tag{20}
$$

After solving the least-square problem (15), follow the scaling coefficients from $A = a$ and $B = b/a$. The resultant scaling coefficients are summarized in Table 4). Figure 5 shows the respective fits and the data, for both configurations individually, and jointly.

Table 4: Least-square coefficients and goodness-of-fit of friction factor scaling (2)

configuration	A	B	R^2 [%]
28 mil	11.640	0.194	99.6
34 mil	11.453	0.185	99.4
collective	11.557	0.190	99.2

The two configuration data sets, as well as their cumulative data set, are excellently captured by equation (2), as indicated by the goodness-of-fit column in Table 4. For cross flow velocities with Reynolds numbers greater than 80, the friction factor accurately scales with $Re^{-\frac{1}{2}}$, independent of the spacer orientation or channel height. The narrow configuration appears to have a slightly greater friction factor. Consequently, the coefficients for the collective data set lie in between these of the wide and the narrow channel.

The slight discrepancy in the values for the coefficient A can be mitigated by introducing the scaling term $(dh/\Delta l)^{\frac{1}{2}}$ in equation (2), suggesting that the friction factor to a greater extent depends on the periodicity of the problem, compared to the Sherwood number.

The orientation coefficient B exhibits marginal variations across configurations, indicating that the $\sin(2\alpha)$ functional captures the orientation dependence well. Comparing coefficient B's value to unity, indicates the significant impact of spacer orientation on the friction factor: The friction factor increases by almost 20%, as the spacer is rotated from 0° to 45°.
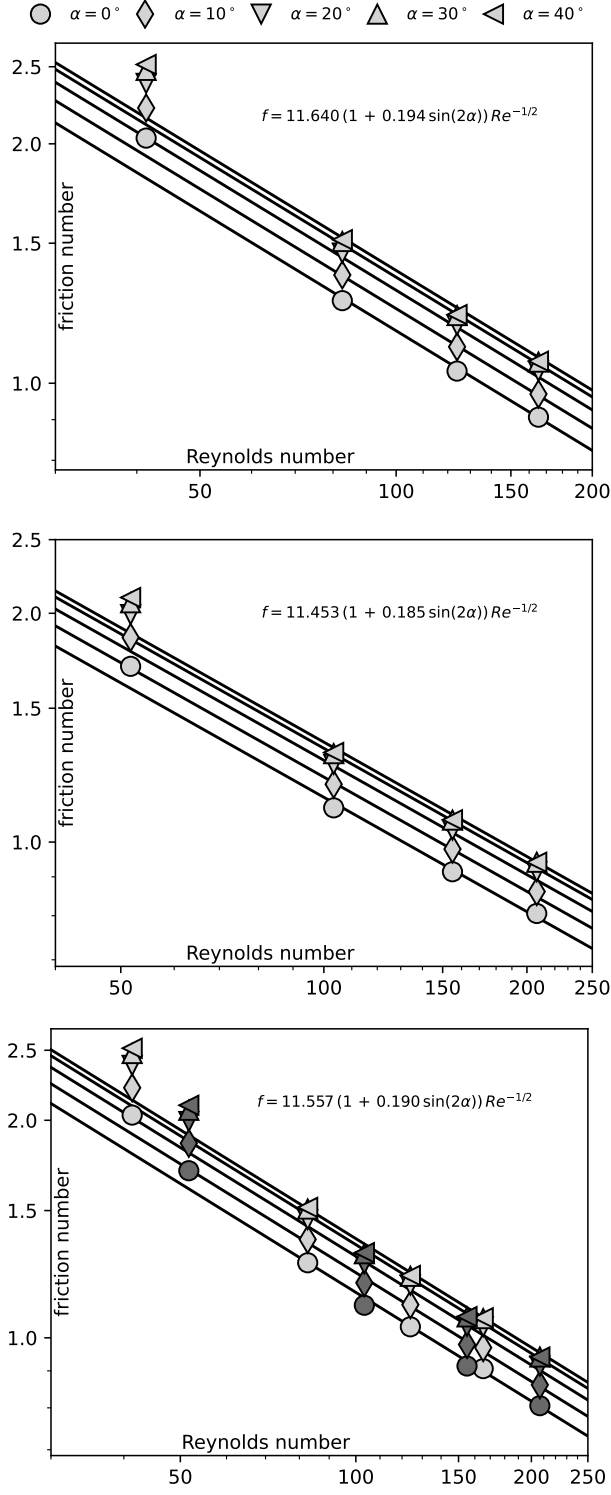
Figure 5: top: d28m, middle: d34m, bottom: both. the low-Reynolds number values were excluded in the respective data fittings.

Empty channel analysis

The Sherwood number follows a scaling relation of the Reynolds number $Sh = A \times Re^{\frac{1}{3}}$ and the least-square solution follows from $A = \frac{X \cdot Z}{X \cdot X}$ with:

$$X = \left(Re_1^{\frac{1}{3}}, Re_2^{\frac{1}{3}}, ..., Re_8^{\frac{1}{3}} \right)$$
$$Z = \left(Sh_1, Sh_2, ..., Sh_8 \right)$$

(21)

The resultant Sherwood number scaling is $Sh = 4.98 \times Re^{\frac{1}{3}}$, with a goodness-of-fit value of $R = 0.985$, indicating an excellent fit. Figure 6 (left) shows the simulation data for the Sherwood number, together with its least-square fit.

The friction factors data are plotted in Fig. 6 (right). Since the friction number enters a transition into a different scaling, for $Re > 200$, these data are not fitted. Instead, the low-Reynolds number values are compared to the reference scaling $f = 10Re^{-1}$. Qualitatively, it can be seen that the low-cross flow data, $Re < 200$ is well captured by this scaling law.
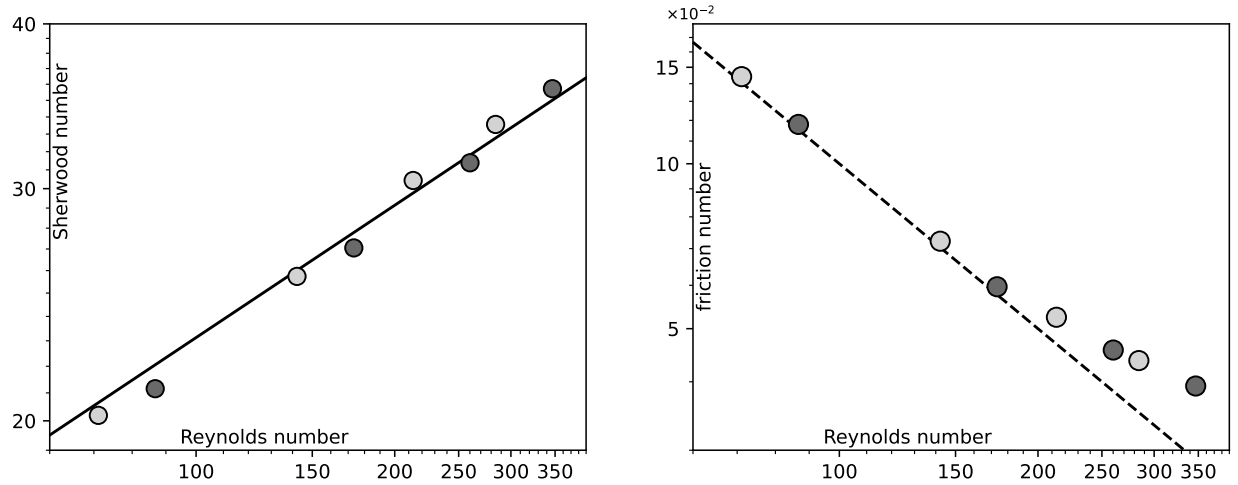

Figure 6: Sherwood empty channel: $Sh = 4.98 \times Re^{1/3}$. friction empty channel: dashed line: $f = 10 \times Re^{-1}$ reference for low rRynolds numbers

4. Conclusion

This study systematically analyzes the scaling relations governing mass transfer and frictional resistance in periodically confined channels, focusing on the influence of flow orientation. The results confirm that the Sherwood number in an empty channel follows a $Re^{1/3}$ scaling, while the spacer-filled channel exhibits a stronger dependence of $Re^{1/2}$, demonstrating the enhanced mixing effect of spacers.

For the friction factor, a transition from a steep laminar regime to a more turbulent-like scaling occurs at $Re < 150$ in the empty channel, but this transition shifts to $Re < 80$ in the spacer-filled channel, indicating an earlier onset of mixing-induced flow resistance. The hydraulic diameter, often used as a universal scaling parameter, proves insufficient for capturing the complex interactions in non-uniform, periodically constrained flows. Since flow orientation significantly affects pressure drop, different geometrical orientations correspond to different effective hydraulic diameters, meaning that a purely geometric definition is inadequate. Instead, the hydraulic diameter must be treated as a function of flow orientation to reflect its role in pressure losses. Crucially, the increase in mass transfer due to orientation comes at the cost of higher frictional resistance, highlighting the need for a trade-off analysis in future optimization studies. These findings underscore the

importance of considering flow orientation effects in process design, as the relationship between transport efficiency and flow resistance is essential for improving energy efficiency and operational performance in confined channel systems.

Together with the recently published study on an algebraic water flux equation, see Tiraferri et al. (2023), the present study is the centerpiece of an update on an earlier work on a numerical process optimization tool, Aschmoneit and Hélix-Nielsen (2020b).

References

Aschmoneit, F.J., Hélix-Nielsen, C., 2020a. 4 - Computational fluid dynamics modeling of forward osmosis processes, in: Basile, A., Cassano, A., Rastogi, N.K. (Eds.), Current Trends and Future Developments on (Bio-) Membranes. Elsevier, pp. 85–111. URL: https://www.sciencedirect.com/science/article/pii/B9780128167779000046, doi:0.1016/B978-0-12-816777-9.00004-6.

Aschmoneit, F.J., Hélix-Nielsen, C., 2020b. OMSD – An open membrane system design tool. Separation and Purification Technology 233, 115975. URL: https://www.sciencedirect.com/science/article/pii/S1383586619326097, doi:10.1016/j.seppur.2019.115975.

Aschmoneit, F.J., Hélix-Nielsen, C., 2021. Submerged-helical module design for pressure retarded osmosis:A conceptual study using computational fluid dynamics. Journal of Membrane Science 620, 118704. URL: https://www.sciencedirect.com/science/article/pii/S0376738820312801, doi:10.1016/j.memsci.2020.118704.

Aschmoneit, F.J., Hélix-Nielsen, C., 2022. Chapter 3 - Application of computational fluid dynamics technique in reverse osmosis/nanofiltration processes, in: Basile, A., Ghasemzadeh, K. (Eds.), Current Trends and Future Developments on (Bio-) Membranes. Elsevier, pp. 63–79. URL: https://www.sciencedirect.com/science/article/pii/B9780128222942000084, doi:10.1016/B978-0-12-822294-2.00008-4.

Benjamin, J., AL Mashrafi, S., Tejada-Martinez, A., Diaz-Elsayed, N., Arias, M.E., Zhang, Q., 2022. Optimizing pressure retarded osmosis spacer geometries: An experimental and CFD modeling study. Journal of Membrane Science 647, 120284. URL: https://www.sciencedirect.com/science/article/pii/S0376738822000333, doi:10.1016/j.memsci.2022.120284.

Bohacek, J., Raudensky, M., Astrouski, I., Karimi-Sibaki, E., 2021. An optimal design for hollow fiber heat exchanger: A combined numerical and experimental investigation. Energy 229, 120571. URL: https://www.sciencedirect.com/science/article/pii/S0360544221008203, doi:10.1016/j.energy.2021.120571.

Focke, W.W., 1983. On the mechanism of transfer enhancement by eddy promoters. Electrochimica Acta 28, 1137–1146. URL: https://www.sciencedirect.com/science/article/pii/001346868380019X, doi:10.1016/0013-4686(83)80019-X.

He, K., Zhang, L.Z., 2019. Fluid flow and heat transfer of cross flow hollow fiber membrane contactors with randomly distributed fibers: A topological study. International Journal of Heat and Mass Transfer 135, 186–198. URL: https://www.sciencedirect.com/science/article/pii/S0017931018351603, doi:10.1016/j.ijheatmasstransfer.2019.01.112.

Mokhtar, I.E., Gurreri, L., Tamburini, A., Cipollina, A., Ciofalo, M., Bouguecha, S.a.T., Micale, G., 2021. CFD prediction of flow, heat and mass transfer in woven spacer-filled channels for membrane processes. International Journal of Heat and Mass Transfer 173, 121246. URL: https://www.sciencedirect.com/science/article/pii/S0017931021003495, doi:10.1016/j.ijheatmasstransfer.2021.121246.

Ng, W.H., Liang, Y.Y., Weihs, G.A.F., 2023. Quantifying the potential of pressure retarded osmosis advanced spacers for reducing specific energy consumption in hybrid desalination. Journal of Water Process Engineering 55, 104197. URL: https://www.sciencedirect.com/science/article/pii/S2214714423007171, doi:10.1016/j.jwpe.2023.104197.

Patankar, S.V., Liu, C.H., Sparrow, E.M., 1977. Fully Developed Flow and Heat Transfer in Ducts Having Streamwise-Periodic Variations of Cross-Sectional Area. Journal of Heat Transfer 99, 180–186. URL: `https://doi.org/10.1115/1.3450666`, doi:10.1115/1.3450666.

Schwager, F., Robertson, P.M., Ibl, N., 1980. The use of eddy promoters for the enhancement of mass transport in electrolytic cells. Electrochimica Acta 25, 1655–1665. URL: `https://www.sciencedirect.com/science/article/pii/0013468680800193`, doi:10.1016/0013-4686(80)80019-3.

Tiraferri, A., Malaguti, M., Mohamed, M., Giagnorio, M., Aschmoneit, F.J., 2023. Standardizing practices and flux predictions in membrane science via simplified equations and membrane characterization. npj Clean Water 6, 1–12. URL: `https://www.nature.com/articles/s41545-023-00270-w`, doi:10.1038/s41545-023-00270-w. number: 1 Publisher: Nature Publishing Group.

Vitagliano, V., Lyons, P.A., 1956. Diffusion Coefficients for Aqueous Solutions of Sodium Chloride and Barium Chloride. Journal of the American Chemical Society 78, 1549–1552. URL: `https://doi.org/10.1021/ja01589a011`, doi:10.1021/ja01589a011. publisher: American Chemical Society.

Winograd, Y., Solan, A., Toren, M., 1973. Mass transfer in narrow channels in the presence of turbulence promoters. Desalination 13, 171–186. URL: `https://www.sciencedirect.com/science/article/pii/S0011916400820433`, doi:10.1016/S0011-9164(00)82043-3.